NANO LETTERS

pubs.acs.org/NanoLett

Letter

Single-Nitrogen–Vacancy NMR of Amine-Functionalized Diamond Surfaces

John M. Abendroth,*[,†] Konstantin Herb,[†] Erika Janitz, Tianqi Zhu, Laura A. Völker, and Christian L. Degen*

Cite This: *Nano Lett.* 2022, 22, 7294–7303

Read Online

ACCESS | Metrics & More | Article Recommendations | Supporting Information

ABSTRACT: Nuclear magnetic resonance (NMR) imaging with shallow nitrogen–vacancy (NV) centers in diamond offers an exciting route toward sensitive and localized chemical characterization at the nanoscale. Remarkable progress has been made to combat the degradation in coherence time and stability suffered by near-surface NV centers using suitable chemical surface termination. However, approaches that also enable robust control over adsorbed molecule density, orientation, and binding configuration are needed. We demonstrate a diamond surface preparation for mixed nitrogen- and oxygen-termination that simultaneously improves NV center coherence times for <10 nm-deep emitters and enables direct and recyclable chemical functionalization via amine-reactive cross-linking. Using this approach, we probe single NV centers embedded in nanopillar waveguides to perform ^{19}F NMR sensing of covalently bound fluorinated molecules with detection on the order of 100 molecules. This work signifies an important step toward nuclear spin localization and structure interrogation at the single-molecule level.

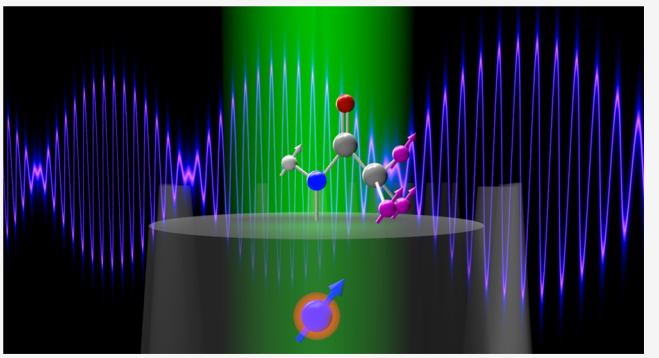

KEYWORDS: *nitrogen–vacancy (NV) center, quantum sensing, magnetometry, nuclear magnetic resonance (NMR), ammonia plasma, surface functionalization*

Elucidating molecular structure at the single- to few-molecule level is an important goal in analytical chemistry, biochemistry, and molecular biology. As a popular structural probe, nuclear magnetic resonance (NMR) spectroscopy enables identification of atomic arrangements and hierarchical ordering in molecules using the resonant frequency of atomic nuclear spins. However, conventional NMR spectroscopy suffers from poor sensitivity due, in part, to intrinsically small nuclear spin polarizations in thermal equilibrium at room temperature.[1] Alternatively, a powerful route to realize highly sensitive nanoscale-NMR employs nitrogen–vacancy (NV) centers in diamond.[2−4] The NV center is a fluorescent crystal defect in diamond composed of a substitutional nitrogen and adjacent vacancy that can act as an atomic-sized sensor for small magnetic moments.[5−7] For sensing nuclear spins at diamond surfaces, it is critical to stabilize shallow (<10 nm-deep) NVs, preserve their coherence properties, and control adsorbed molecule density, orientation, and binding configuration.

Functionalization of the diamond surface is possible using a variety of chemical approaches,[8−11] but such modifications can be detrimental to near-surface NVs. Charge state conversion from the useful negatively charged state to the neutral state due to surface charge traps or band bending renders the defect ineffective for magnetic sensing.[12−14] Moreover, detection sensitivity is worsened in shallow NVs from surface noise.[15−17] Promising chemical approaches to minimize surface noise and charge-state instability include fluorination,[18] nitrogen termination,[19−22] or oxygen termination.[23−27] On widely used oxygen-terminated diamond, carboxyl groups enable attachment of molecules of interest using carbodiimide cross-linker chemistry.[28,29] However, surface passivation and density of adsorbed analytes are difficult to control when limited solely by the native surface concentration of residual chemically addressable moieties. Furthermore, coverage of carboxyl groups is typically low on oxidized surfaces,[30] and various oxidation protocols yield different compositions depending on surface roughness and crystallographic orientation.[11,31,32]

Atomic layer deposition (ALD) may be used to grow 1−2 nm-thick adhesion layers for dense molecular self-assembly. Recent reports have used ALD with chemical modification via

Received: February 9, 2022
Revised: August 9, 2022
Published: September 7, 2022

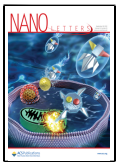

https://doi.org/10.1021/acs.nanolett.2c00533
Nano Lett. 2022, 22, 7294–7303

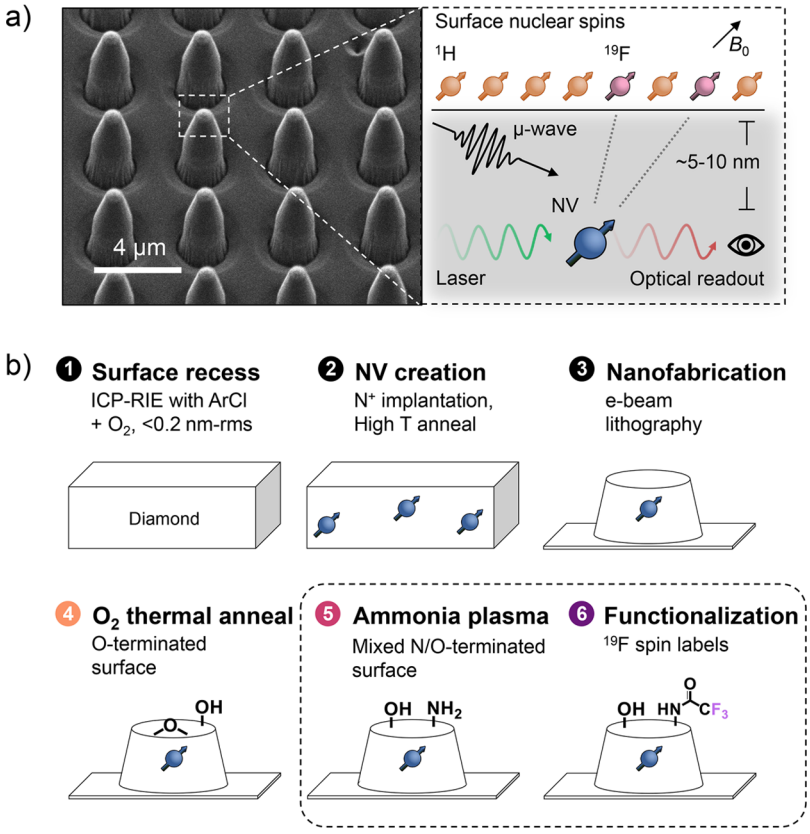

Figure 1. (a) Experimental overview for conducting surface NMR with single NV centers. Left: scanning electron micrograph of a representative diamond nanopillar waveguide array hosting single NV centers. Right: scheme illustrating sensing of surface nuclear spins by shallow NV centers. (b) Workflow of sample preparation and chemical functionalization of diamond surfaces. The dotted box highlights the focus of this work.

phosphate or silane anchoring to enable NMR detection of molecular films in ensemble NV NMR measurements[33] and to develop biocompatible surface architectures for NV sensing.[34] Still, this method can result in decreased coherence of near-surface NVs and adds distance between the NV sensor spin and target surface spins. Moreover, the dipolar interaction scales inversely with the third power of this separation, further motivating direct molecular attachment.[35−39] Dense molecular assemblies of silane molecules may instead be formed without adhesion layers on oxygen-terminated diamond, anchored to hydroxyl groups.[40−42] Surface NMR sensing of ^{19}F is possible with shallow NVs without ALD layers for vapor-deposited films of trimethoxy(3,3,3-trifluoropropyl)silane and films of (3-aminopropyl)trimethoxysilane with subsequent amine-reactive cross-linking of trifluoromethyl tags (SI Figure S1). However, multilayer formation in silane films and degradation under aqueous conditions and air exposure are major challenges.[43−47] Improved surface treatments are necessary that simultaneously enable predictable molecular attachment and stabilization of shallow NV sensors.

Here, we demonstrate direct chemical functionalization of mixed nitrogen- and oxygen- (N/O−) terminated diamond for surface NMR spectroscopy with single NV centers (Figure 1). Starting with thermally annealed O-terminated diamond, the composition of mixed N/O surface termination was controlled with exposure to ammonia (NH_3) plasma. We show covalent and reversible surface functionalization of amine groups introduced by plasma exposure using derivatization. With short (20 s) plasma exposure times, mixed N/O-terminated surfaces improved the coherence time of <10 nm-deep NVs compared to only O_2-annealed surfaces. Subsequently, we employed *N*-hydroxysuccinimide (NHS) ester cross-linking to functionalize the diamond surface with fluorinated molecules and detected surface-bound ^{19}F spins. Within the sensing volume of each NV, we estimate detection of fewer than 200 molecules. This surface functionalization demonstrates the generalizability of our immobilization protocol and the persistent stability of shallow NVs after molecular attachment.

Bulk and membrane samples with (100) surface termination (the latter for nanofabrication of pillar arrays) were recessed using Ar/Cl_2 and O_2 inductively coupled plasma reactive ion etching (ICP-RIE, Step 1, Figure 1b), yielding <0.2 nm-rms surface roughness (SI Figure S2). To create shallow NVs, recessed diamond samples were implanted with $^{15}N^+$ ions (Step 2, Figure 1b) with energies of 5 or 7 keV and fluences of 10^9 cm^{-2}, yielding an expected average implantation depth of 8.0(31) and 10.8(40) nm, respectively (SI Figure S3).[48] Annealing at 880 °C for 2 h under high vacuum (<5 × 10^{-8} mbar) converted implanted $^{15}N^+$ ions into NV centers. Nanopillar arrays were then patterned on membrane samples via electron-beam lithography (Step 3, Figure 1b) for higher photoluminescence collection efficiency and to provide a map to selectively address and revisit the same NVs for repeated characterization.[49]

Samples were subsequently annealed under an O_2 atmosphere at 460 °C to remove graphitic carbon and to generate fully O-terminated diamond surfaces (Step 4, Figure 1b). Using an analogous O_2-annealing procedure, Sangtawesin et al. demonstrated improvements in coherence (T_2) times of shallow NVs up to four times compared to acid-cleaned

https://doi.org/10.1021/acs.nanolett.2c00533
Nano Lett. 2022, 22, 7294−7303

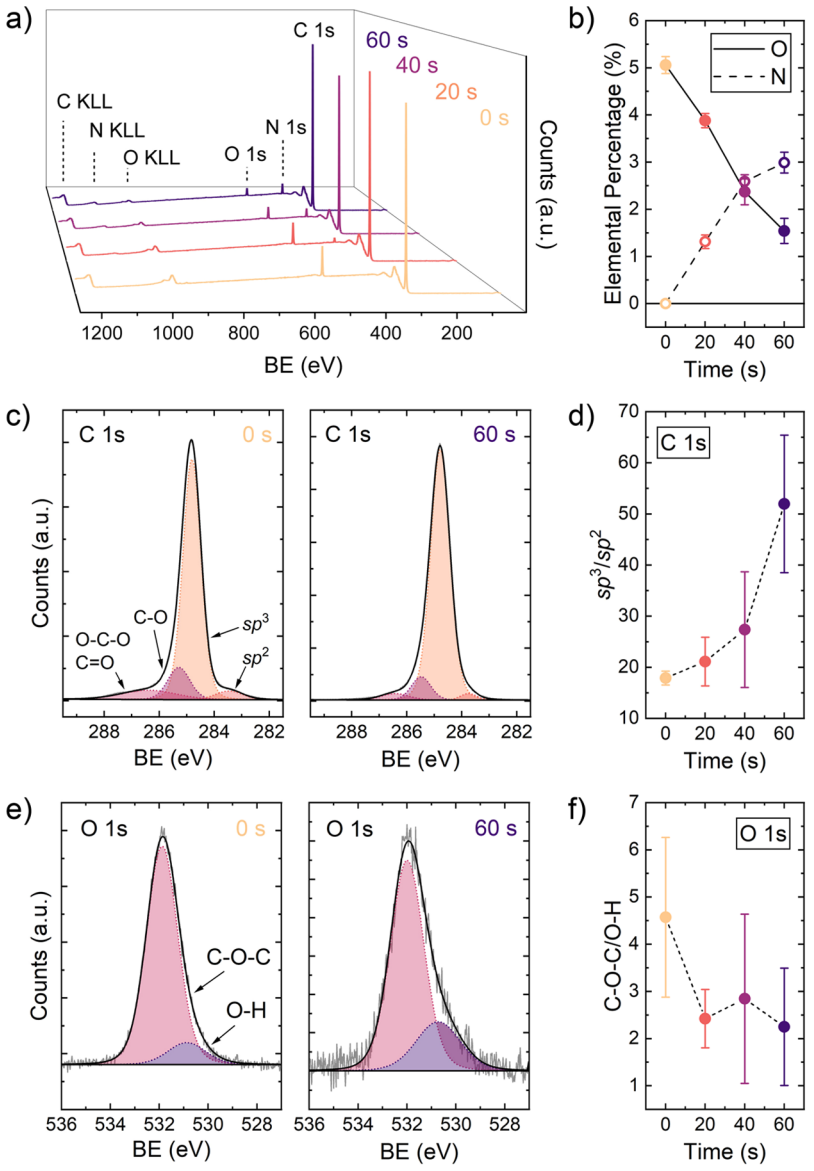

Figure 2. Characterization of diamond surfaces with X-ray photoelectron spectroscopy. (a) Representative survey scans of O_2-annealed diamond with increasing exposure time to NH_3 plasma. Binding energies (BE) of C, O, and N 1s core electrons and Auger signatures are indicated. (b) Elemental percentage of oxygen and nitrogen within the sampling depth as a function of exposure time. (c) Representative high-resolution C 1s scans before (0 s) and after (60 s) plasma exposure. (d) Ratio of sp^3/sp^2 components from the fitting of C 1s signals. (e) Representative high-resolution O 1s scans before (0 s) and after (60 s) plasma exposure. (f) Ratio of C−O−C (ether) assignment at 531.9 eV and O−H (hydroxyl) contribution at ∼1 eV lower binding energy from fitting of O 1s signals. Error bars represent standard deviation from $N = 3$ samples for each condition.

diamond surfaces, which was attributed to an ordered, predominantly ether-terminated surface.[25] We observed an improvement in NV optical contrast using both continuous wave (cw) and pulsed optically detected magnetic resonance (ODMR) measurements, and factor-of-two improvement in coherence and Rabi decay times of NVs following O_2-annealing (SI Figure S4).

Next, we incorporated additional reactive amine terminal groups for subsequent molecular attachment by introducing a 50 W *rf* of 13.56 MHz NH_3 plasma treatment to O_2-annealed surfaces for mixed N/O-termination (Step 5, Figure 1b). Importantly, surfaces remained smooth with no evidence of roughening or contamination by physisorbed species left by the plasma process (SI Figure S5). Controlled exposure time mitigates conversion to a fully amine-terminated surface which is known to exhibit negative electron affinity and can be detrimental for NV stability.[50] We note that alternative diamond amination procedures using NH_3, N_2, or mixed-source plasmas have been developed previously, but either with hydrogen-terminated diamond as a starting surface or without characterizing their influence on the photophysical properties of near-surface NVs.[51−55]

Changes to the chemical composition of the surfaces exposed to 0, 20, 40, and 60 s of NH_3 plasma were characterized using X-ray photoelectron spectroscopy (XPS) on bulk O_2-annealed diamond samples. A decrease in elemental percentage of O in the sampling depth (about ≤6 nm) was accompanied by an increase in N to 3% after 60 s (Figure 2a,b). These percentages were obtained by integration of O 1s, N 1s, and C 1s signals after adjusting for

https://doi.org/10.1021/acs.nanolett.2c00533
Nano Lett. 2022, 22, 7294−7303

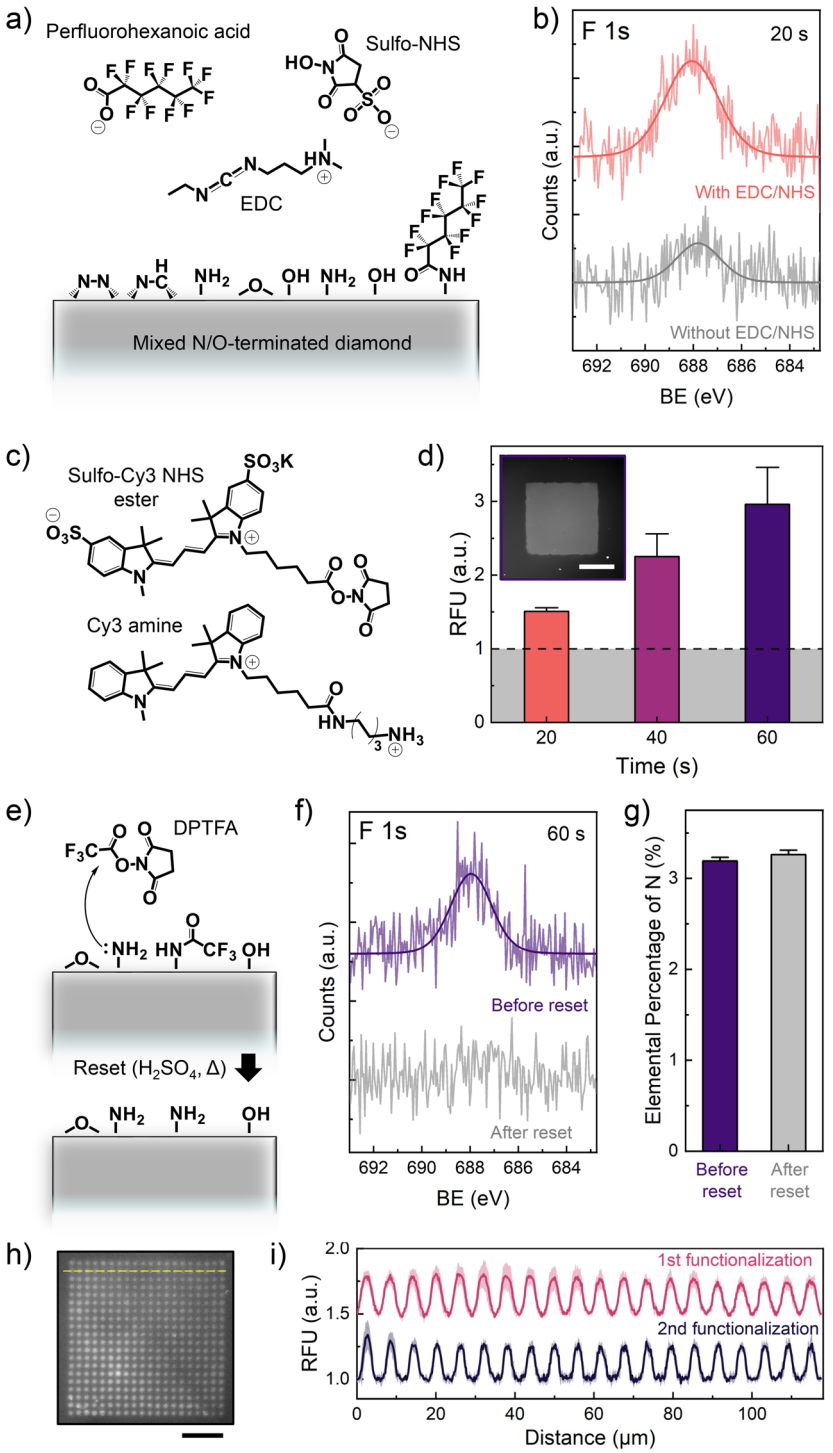

Figure 3. Characterization of diamond surface functionalization. (a) Schematic of surface functionalization with perfluorohexanoic acid with *N*-hydroxysulfo-succinimide sodium salt (sulfo-NHS), and *N*-(3-(dimethylamino)propyl)-*N*′-ethylcarbodiimide hydrochloride (EDC). (b) Representative high-resolution F 1s scans following surface incubation with perfluorohexanoic acid in the presence or absence of EDC and sulfo-NHS. (c) Chemical structures of the fluorescent dyes sulfo-Cy3 NHS ester and Cy3 amine used for testing surface functionalization via fluorescence microscopy. (d) Fluorescence intensity measured as relative fluorescence units (RFU) of patterned square regions exposed to NH_3 plasma over oxygen-only terminated background regions (RFU = 1) following incubation with sulfo-Cy3 NHS ester. $N = 5$ per condition. Error bars represent standard errors of the means. Inset shows a representative fluorescence microscopy image of a sulfo-Cy3 NHS ester dye-functionalized square region exposed to 60 s plasma (scale bar, 0.2 mm). (e) Schematic of surface functionalization with 2,5-dioxopyrrolidin-1-yl 2,2,2-trifluoroacetate (DPTFA) and reset by incubating with 75% H_2SO_4 at 50 °C for 30 min. (f) Representative high-resolution F 1s scans before and after surface reset. (g) Elemental percentage of nitrogen within the sampling depth before and after surface reset. $N = 5$ per condition. (h) Representative fluorescence microscopy image of a patterned array of sulfo-Cy3 NHS ester dye-functionalized regions exposed to 60 s plasma (scale bar, 30 μm). (i) Fluorescence linescans (average of $N = 6$ per condition) from patterned regions exposed to 60 s plasma on a diamond surface after sulfo-Cy3 NHS ester functionalization before reset and after a second functionalization. Top scan shows the first functionalization. Bottom scan shows after reset and a second functionalization. Errors represent standard deviation.

https://doi.org/10.1021/acs.nanolett.2c00533
Nano Lett. 2022, 22, 7294−7303

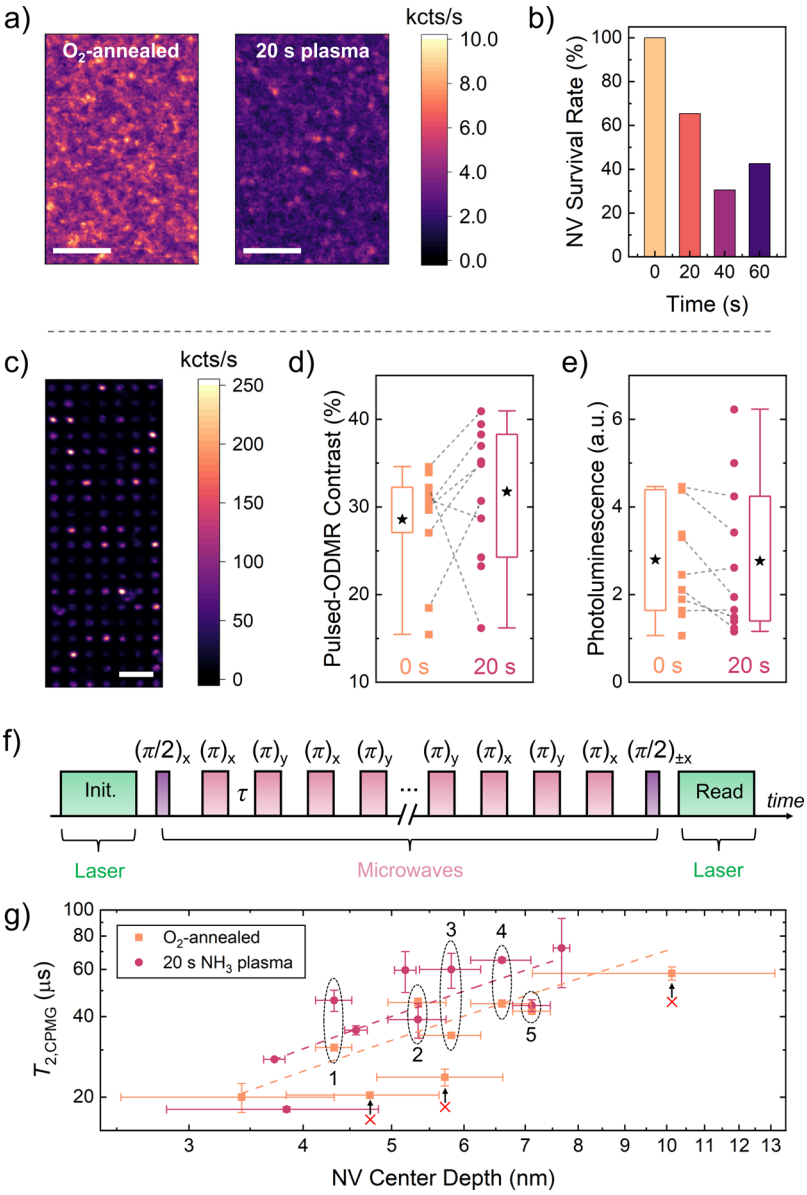

Figure 4. Comparison of NV center properties before and after exposure to NH_3 plasma. (a) Representative confocal fluorescence image of a bulk diamond surface containing shallow NV centers before plasma exposure (left) and after 20 s (right). Scale bars are 5 μm. (b) Survival rate of NV centers after different plasma exposure times. (c) Representative confocal fluorescence image of a nanopillar array hosting NV centers in a diamond membrane. Scale bar is 10 μm. (d) Pulsed-ODMR contrast and (e) photoluminescence intensity of NV centers in nanopillar waveguides before and after plasma treatment. In the box and whisker plots, black stars show the mean values of the data. Boxes comprise the middle 25−75% of the data. Whiskers extend to 1.5× this interquartile range. Dotted gray lines connect the same NV centers characterized before and after plasma exposure. (f) Dynamical decoupling spectroscopy sequence for detecting nuclear spin signals. (g) Coherence time ($T_{2,\mathrm{CPMG}}$ with 128 pulses) of NV centers as a function of depth within the diamond. Red crosses indicate NV centers from which no ODMR signal could be measured following plasma treatment. Dashed lines are guides for the eye. Data points representing the same NV centers characterized both before and after plasma exposure are indexed. Panels a and b correspond to data collected from bulk crystals, while panels c−g correspond to data collected from nanopillar arrays on diamond membranes.

photoionization cross sections of the core electron species.[56] The surface concentration (σ_N) of N atoms was estimated to range from 4.9(2) N atoms nm^{-2} for 20 s exposure to 12.1(2) N atoms per nm^2 for 60 s exposure using[55]

$$\frac{I_N}{I_C} = \frac{\mu_N A_w \sigma_N}{\mu_C \rho_d N_A \lambda_m} \quad (1)$$

where I_N/I_C is the ratio of integrated N 1s and C 1s signal intensities with photoelectron cross sections of μ_N and μ_C,[56] A_w is the atomic weight of carbon, ρ_d is the density of diamond (3.52 g cm^{-3}), N_A is Avogadro's number, and λ_m is the mean free path of C 1s photoelectrons in diamond (~2 nm for 1486.6 eV photon energy).[57] The value of σ_N saturates with longer plasma exposure at about 15 N atoms nm^{-2} (SI Figure S6). The emergent N 1s peak position at 398.4 eV suggests predominately single-bonded C−N and/or double-bonded C═N, while nitrile groups may be excluded.[19,58] Analysis of high-resolution C 1s spectra shows a dominant peak at 284.8 eV assigned to sp^3 carbon, a shoulder at ~1 eV lower binding energy attributed to sp^2 carbon, and satellite peaks at higher binding energy due to carbon−oxygen binding (Figure

https://doi.org/10.1021/acs.nanolett.2c00533
Nano Lett. 2022, 22, 7294−7303

2c).[25,59] The NH_3 plasma treatment reduced the already low amount of sp^2 carbon on the diamond surfaces with increasing exposure time (Figure 2d). The high-resolution O 1s signals can be fit with a C−O−C (ether) assignment at 531.9 eV and C−O−H (hydroxyl) contribution at ∼1 eV lower binding energy (Figure 2e).[25] The relative ratio of these two peaks for O_2-annealed diamond is ∼5:1, and decreases to ∼2:1 after 60 s plasma exposure (Figure 2f).

The presence of reactive amines on the mixed N/O-terminated diamond surface was determined by derivitization. Complementary characterization using XPS and fluorescence microscopy was used to test covalent attachment, control over surface density, and recyclability (Figure 3). First, diamond surfaces treated with 20 s NH_3 plasma were incubated with perfluorohexanoic acid in the presence or absence of equimolar amounts of *N*-hydroxysulfo-succinimide sodium salt (sulfo-NHS), and *N*-(3-(dimethylamino)propyl)-*N*′-ethylcarbodiimide hydrochloride (EDC) (Figure 3a). High-resolution F 1s spectra exhibit higher intensity when sulfo-NHS and EDC were present, which facilitate covalent amine-reactive cross-linking as opposed to nonspecific binding alone (Figure 3b). Second, different regions of the diamond surface were patterned with 20, 40, or 60 s exposure time and incubated with sulfo-Cy3 dye molecules containing an activated NHS group (Figure 3c). Regions were imaged and the fluorescence intensity, measured as relative fluorescence units (RFU), was calculated by normalization against unpatterned O_2-annealed background regions. Increasing RFU was observed with increasing exposure time up to 60 s (Figure 3d). With longer exposure times, relative fluorescence intensity decreased, which suggests that available amine groups for functionalization are converted into different nitrogen-based surface terminations (SI Figure S7). These results indicate tunability of available amine groups and thereby the surface density of adsorbed molecules. No pattern was detected when the dye lacked the NHS ester (SI Figure S8). Third, this functionalization is reversible. Surfaces can be reset by treating with 75% H_2SO_4 at 50 °C for 30 min to break the amide bonds formed between the adsorbed molecules and aminated surface. We tested this process on a sample explosed to NH_3 plasma and functionalized with 2,5-dioxopyrrolidin-1-yl 2,2,2-trifluoroacetate (DPTFA) (Figure 3e). Specific functionalization was confirmed by detection of fluorine via XPS (SI Figure S9). Following the reset, the F 1s signal from functionalizion was no longer visible, while the N elemental percentage remained unchanged (Figure 3f,g). Moreover, such surfaces can be refunctionalized. We compared fluorescence from surfaces that were first exposed to 60 s plasma and subsequently patterned with sulfo-Cy3 NHS ester dye molecules before and after resetting. (Figure 3h). Comparable RFU values were measured, indicating that surfaces can thus be refunctionalized without repeated plasma treatment (Figure 3i).

We next tested how the NH_3 plasma treatment affects the sensing properties of shallow NV centers. Figure 4a shows representative confocal fluorescence images of bulk diamond surfaces containing individually resolvable NVs before and after 20 s plasma exposure. The plasma treatment caused background fluorescence to decrease, making it easier to distinguish fluorescent NV centers from bright surface impurities. Individual NVs were identified and characterized using ODMR. In ODMR, NVs are first illuminated with a green laser (λ = 532 nm) to polarize the electron spin into the m_s = 0 state. Applying a subsequent microwave field at the Larmor frequency of the electron spin drives transitions between the optically polarized m_s = 0 (bright) state and the m_s = ±1 (dark) states. Finally, readout is performed by integrating the emitted photons during a second green laser pulse. Measurement sensitivity scales linearly with ODMR contrast, which is defined as the ratio of integrated fluorescence of the bright vs dark states.[6]

Increased plasma exposure time was accompanied by a decrease in the number of NV centers that display an ODMR signal (Figure 4b). We defined the NV survival rate as the ratio of emitters displaying an ODMR signal per scan area before and after plasma exposure (SI Figure S10). Approximately two-thirds of NVs remained following 20 s plasma exposure, which dropped below 50% after 40 and 60 s. Consequently, we opted to use nanostructured diamond membranes for further testing such that we could track the same NVs before and after treatment. Figure 4c shows a representative fluorescence map of one nanopillar array after a 20 s plasma treatment. Analogous to bulk samples, a decrease in fluorescence background was observed, in addition to a decrease in the number of pillars containing NV candidates with detectable ODMR signals. Encouragingly, no significant difference in the mean pulsed-ODMR contrast nor the mean photoluminescence of NVs was determined before versus after 20 s plasma exposure (Figure 4d,e).

Next, we compared coherence properties of NV centers using a Carr−Purcell−Meiboom−Gill-type (CPMG) dynamical decoupling protocol (Figure 4f).[60,61] After an initial $\pi/2$ pulse, a train of π-pulses refocuses the spin. A final $\pi/2$ pulse maps the coherence back to the initialized bright state. Increasing the evolution time between π-pulses results in a signal decay with time constant $T_{2,\mathrm{CPMG}}$. To compensate for brightness variations, we collected reference traces of an initialization of the m_s = 0 and m_s = −1 state in parallel. This sequence also allows one to perform NMR spectroscopy; by tuning the interpulse delay of the π-pulses to half the Larmor period, one can perform a lock-in measurement of the magnetic variance generated by external nuclear spins.[62] Quantifying the signal, we estimated the root-mean-square value of the *B*-field fluctuations produced by external spins, which was then used to infer NV depths. Calculation of B_{rms} was performed both using a Monte Carlo method as well as an analytic model for comparison.[16,63,64] From the extracted B_{rms} we inferred the depth by inverting[16]

$$B_{\mathrm{rms}}^2(d) = \frac{5\mu_0^2\hbar^2\gamma_{\mathrm{H1}}^2}{1536\pi}\frac{\rho}{d^3}\left(1 - \frac{d^3}{(d+\Delta)^3}\right) \approx (1.14\,\mu\mathrm{T\ nm^3})^2\frac{\rho}{d^3}\left(1 - \frac{d^3}{(d+\Delta)^3}\right) \quad (2)$$

where μ_0 denotes the magnetic field constant, $\hbar$ is the reduced Planck's constant, $\gamma_{\mathrm{H1}} = 2\pi(42.58\ \mathrm{MHz\ T^{-1}})$ is the gyromagnetic ratio of protons, ρ is the proton-layer density, Δ is the thickness of this layer, and d is the NV-center depth. For the depth calculation of each NV, we assumed an adsorbed water layer (proton density of ρ = 60 $\mathrm{nm^{-3}}$) of Δ = 1.3 nm based on the mean Δ value from corroborating depth measurements using microscope immersion oil with known ρ (SI Figure S11).[16,63−68]

The $T_{2,\mathrm{CPMG}}$ coherence times are shown as a function of NV depth in Figure 4g. We observed a monotonic decrease in NV coherence time with increasing proximity to the surface,

https://doi.org/10.1021/acs.nanolett.2c00533
Nano Lett. 2022, 22, 7294−7303

consistent with previous reports.[25,34,69−71] Promisingly, the $T_{2,CPMG}$ values were larger on average after 20 s plasma exposure. For five NVs directly compared before and after plasma treatment (Table 1), we observed increases in $T_{2,CPMG}$ by as much as 1.8(3) times. Additionally, from the data set characterized prior to plasma exposure, we could not measure an ODMR signal from three NV centers following 20 s plasma, indicated by red crosses in Figure 4g. We note that these NVs with calculated depths of 4.7(9), 5.7(9), and 10.1(30) nm, each exhibited below-average coherence times, suggesting that while the plasma reduces the number of observed NVs (Figure 4b), it preserves those with the highest stability and sensitivity for performing surface NV NMR measurements.

Table 1. Depth[a] and $T_{2,CPMG}$ for NV Centers Characterized before and after 20 s NH_3 Plasma Exposure

		$T_{2,CPMG}$ (μs)	
	depth[a] d (nm)	O_2-annealed	NH_3 plasma
NV 1	4.3(2)	30.6(9)	46.0(42)
NV 2	5.3(4)	45.1(17)	39.0(58)
NV 3	5.8(4)	34.0(8)	60.0(9)
NV 4	6.6(5)	44.8(14)	65.0(13)
NV 5	7.1(4)	41.9(7)	44.0(22)

[a]Depth values are calculated from the average of B_{rms} measurements before and after plasma treatment (Table S1).

Finally, we tested our N/O-termined diamond NV sensing platform for nanoscale-NMR of surface-bound molecules (Step 6, Figure 1b) using functionalization with DPTFA (Figure 5a,b) and perfluorohexanoic acid (SI Figure S12). Surface NV NMR spectra shown in Figure 5a correspond to the same NV center (indexed as NV 4) measured after O_2-annealing, 20 s plasma treatment, and functionalization with DPTFA (Steps 4−6, Figure 1b). Prior to attachment of trifluoromethyl moieties to the surface, the dynamical decoupling spectrum shows only dips in contrast at the frequency corresponding to ^{1}H spins, attributed mainly to an adsorbed water layer. After exposure to 20 s plasma, an improvement in coherence time of the NV is evident by reduced signal decay with decreasing frequency which produces a further pronounced proton signal. Following attachment of trifluoromethyl tags, a second dip appears, which can be assigned to ^{19}F surface spins. Assignment in the NV NMR spectra is validated by measuring multiple NV centers independently and at distinct magnetic field biases, which shifts the Larmor frequencies of ^{1}H and ^{19}F spins (Figure 5b,c).

To estimate the number of molecules that contributed to the detected fields, we analyzed the molecular surface density via nanoscale-NMR following functionalization with DPTFA using two distinct NVs (indexed as NV 4 and NV 6) (Figure 5b). For NV 4, we find a B_{rms} of 245(5) nT at the ^{1}H frequency and 102(5) nT at the ^{19}F frequency. For NV 6, we find 331(12) and 163(7) nT for these two resonances, respectively. Using eq 2, we calculate the corresponding NV depths from the proton signals to be 6.6(5) nm and 6.7(2) nm.[16] Note that for NV 4, the three B_{rms} values from before and after 20 s plasma exposure and after functionalization were averaged to calculate the depth (SI Table S1). These depths are subsequently used to determine ρ_{2D}, the density of the 2D layer of ^{19}F atoms, via

$$B_{rms}^2 = \frac{5\mu_0^2(\gamma_{F19}\hbar)^2}{512\pi d^4}\rho_{2D} = (1.86\ \mu T\ nm^3)^2\frac{\rho_{2D}}{d^4} \quad (3)$$

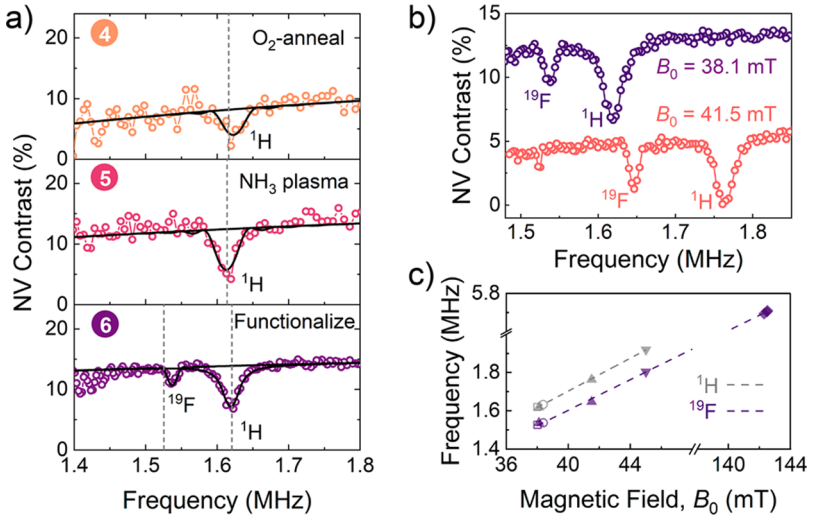

Figure 5. NV NMR sensing of surface nuclear spins. (a) Representative ^{1}H and ^{19}F NV NMR data from the same NV center during surface treatment. Top: after oxygen annealing. Middle: after 20 s ammonia plasma exposure. Bottom: after functionalization with 2,5-dioxopyrrolidin-1-yl 2,2,2-trifluoroacetate (DPTFA). Dotted vertical lines indicate expected positions of ^{19}F and ^{1}H resonance frequencies. The numbers 4, 5, and 6 refer to process steps in Figure 1. (b) NV NMR data collected at two bias fields B_0. Top and bottom traces (indexed as NV 4 and NV 6, respectively) were recorded using two different NV centers. For the top trace, the ^{1}H and ^{19}F resonances are at 1619(1) and 1537(1) kHz, respectively. For the bottom trace these frequencies are at 1764(1) and 1647(1) kHz, respectively. Signal traces in (b) were averaged for 10 h; 384 decoupling pulses were used. (c) Measured ^{1}H and ^{19}F resonance frequencies as a function of applied magnetic field for varying surface functionalization conditions used in this work as follows: Open squares, O_2-annealed, trimethoxy(3,3,3-trifluoropropyl)silane (TMTFS); closed triangles, 20 s NH_3 plasma, DPTFA; open circles, O_2-annealed, (3-aminopropyl)-trimethoxysilane (APTMS) + DPTFA; closed inverted triangles, 60 s NH_3 plasma, DPTFA; closed diamonds, 20 s NH_3 plasma, perfluorohexanoic acid. Samples functionalized with perfluorohexanoic acid were coated with deuterated glycerol, therefore no ^{1}H signal could be detected. Slopes obtained from linear fits (dashed lines) of the full data sets in panel c show agreement with expected gyromagnetic ratios within experimental error (43.03(56) MHz T^{-1} for ^{1}H and 40.02(6) MHz T^{-1} for ^{19}F).

https://doi.org/10.1021/acs.nanolett.2c00533
Nano Lett. 2022, 22, 7294−7303

where $\gamma_{F19} = 2\pi(40.078\ \text{MHz T}^{-1})$ is the gyromagnetic ratio of ^{19}F. We estimate the surface density of ^{19}F to be 6(2) $^{19}F\ nm^{-2}$ and 14(2) $^{19}F\ nm^{-2}$ for NV 4 and NV 6, respectively. Since each attached subunit contains three fluorine atoms per molecule, this corresponds to molecular surface densities of 1.9(6) and 4.9(7) molecules nm^{-2}. These surface densities are consistent with surface concentration of N atoms determined via XPS (4.9(2) atoms nm^{-2} for 20 s NH_3 plasma). The detection volume of an NV center at depth d can be defined as the region producing the first 70% of the signal ($A = 0.735\ d^2$) (SI Figure S13).[3,16] Within this detection volume, we calculate that fewer than 200 molecules contributed to the detected fields by each NV center (SI Table S2).

In summary, we demonstrate a diamond surface preparation strategy that enables direct chemical functionalization of amine groups while improving coherence times of near-surface NV centers for surface NMR spectroscopy. Mixed N/O-terminated surfaces are prepared by thermal annealing under O_2 at elevated temperature and subsequent exposure to NH_3 plasma. This process yields robust and reproducible control over N and O elemental percentages on diamond surfaces. Furthermore, we show covalent and reversible functionalization of aminated surfaces with tunable molecular surface density. We identify an experimental regime in which two-thirds of shallow NV centers are preserved following NH_3 plasma treatment with improved sensing properties compared to O_2-annealed surfaces. We find significant reduction in background luminescence and up to 1.8(3) times improvement in coherence times of near-surface NV centers. Finally, we functionalize fluorinated molecules to surface-bound amine groups and perform NMR spectroscopy at the few-molecule (<200 molecules) regime using dynamical-decoupling noise spectroscopy with single NV centers. The presented approach enables a precise preparation of molecular systems of interest at diamond surfaces that may be applied for emergent NV-center-based quantum sensing of chemical functionality.[72−75]

■ ASSOCIATED CONTENT

Supporting Information

The Supporting Information is available free of charge at https://pubs.acs.org/doi/10.1021/acs.nanolett.2c00533.

Additional materials and experimental methods, as well as additional data used to evaluate the conclusions in the paper; Figures S1−S15 and Tables S1 and S2 show data related to XPS characterization and NV NMR with silanized surfaces, SRIM (The Stopping and Range of Ions in Matter) calculations, atomic force microscopy images, additional characterization of surface functionalization, characterization of NV centers following thermal annealing under oxygen, additional characterization of NV centers following exposure to ammonia plasma and chemical functionalization, integration of the sensitive slice on the surface above each NV center for NMR measurements, and estimated errors from magnetic field measurements and NV center depths (PDF)

■ AUTHOR INFORMATION

Corresponding Authors

John M. Abendroth − *Department of Physics, ETH Zurich, 8093 Zurich, Switzerland;* orcid.org/0000-0002-2369-4311; Email: jabendroth@phys.ethz.ch

Christian L. Degen − *Department of Physics, ETH Zurich, 8093 Zurich, Switzerland;* orcid.org/0000-0003-2432-4301; Email: degenc@ethz.ch

Authors

Konstantin Herb − *Department of Physics, ETH Zurich, 8093 Zurich, Switzerland*

Erika Janitz − *Department of Physics, ETH Zurich, 8093 Zurich, Switzerland*

Tianqi Zhu − *Department of Physics, ETH Zurich, 8093 Zurich, Switzerland*

Laura A. Völker − *Department of Physics, ETH Zurich, 8093 Zurich, Switzerland*

Complete contact information is available at: https://pubs.acs.org/10.1021/acs.nanolett.2c00533

Author Contributions

†J.M.A. and K.H. contributed equally to this work.

Author Contributions

J.M.A., K.H., and C.L.D. conceived and designed the experiments. T.Z. developed the nanostructure fabrication. Data were collected by J.M.A., K.H., and E.J. All authors discussed the results. The manuscript was cowritten by J.M.A. and K.H. with assistance by E.J., T.Z., L.A.V., and C.L.D.

Notes

The authors declare no competing financial interest.

■ ACKNOWLEDGMENTS

The authors thank Dr. Andrea Arcifa from EMPA and Dr. Viraj Damle and Dr. Jan Rhensius from QZabre AG for insightful discussions and their help, and gratefully acknowledge ScopeM and FIRST Center for Micro- and Nanoscience at ETH Zurich for their support and assistance. This work was supported by Swiss National Science Foundation (SNSF) Project Grant 200020 175600, the National Center of Competence in Research in Quantum Science and Technology (NCCR QSIT, Grant 51NF40_185902), and the Advancing Science and TEchnology thRough dIamond Quantum Sensing (ASTER-IQS) program, Grant 820394, of the European Commission. J.M.A. acknowledges funding from an ETH Zurich Career Seed Grant and from a SNSF Ambizione Grant [PZ00P2_201590], and E.J. acknowledges support from a Natural Sciences and Engineering Research Council of Canada (NSERC) postdoctoral fellowship (PDF-558200-2021).

■ REFERENCES

(1) Lee, J. H.; Okuno, Y.; Cavagnero, S. Sensitivity Enhancement in Solution NMR: Emerging Ideas and New Frontiers. *J. Magn. Reson.* **2014**, *241*, 18−31.

(2) Mamin, H. J.; Kim, M.; Sherwood, M. H.; Rettner, C. T.; Ohno, K.; Awschalom, D. D.; Rugar, D. Nanoscale Nuclear Magnetic Resonance with a Nitrogen-Vacancy Spin Sensor. *Science* **2013**, *339*, 557−560.

(3) Staudacher, T.; Shi, F.; Pezzagna, S.; Meijer, J.; Du, J.; Meriles, C. A.; Reinhard, F.; Wrachtrup, J. Nuclear Magnetic Resonance Spectroscopy on a (5-Nanometer)^3 Sample Volume. *Science* **2013**, *339*, 561−563.

(4) Aslam, N.; Pfender, M.; Neumann, P.; Reuter, R.; Zappe, A.; Fávaro de Oliveira, F.; Denisenko, A.; Sumiya, H.; Onoda, S.; Isoya, J.; Wrachtrup, J. Nanoscale Nuclear Magnetic Resonance with Chemical Resolution. *Science* **2017**, *357*, 67−71.

(5) Jelezko, F.; Gaebel, T.; Popa, I.; Gruber, A.; Wrachtrup, J. Observation of Coherent Oscillations in a Single Electron Spin. *Phys. Rev. Lett.* **2004**, *92*, 076401.

(6) Schirhagl, R.; Chang, K.; Loretz, M.; Degen, C. L. Nitrogen-Vacancy Centers in Diamond: Nanoscale Sensors for Physics and Biology. *Annu. Rev. Phys. Chem.* **2014**, *65*, 83−105.
(7) Gali, Á. *Ab initio* Theory of the Nitrogen-Vacancy Center in Diamond. *Nanophotonics* **2019**, *8*, 1907−1943.
(8) Härtl, A.; Schmich, E.; Garrido, J. A.; Hernando, J.; Catharino, S. C. R.; Walter, S.; Feulner, P.; Kromka, A.; Steinmüller, D.; Stutzmann, M. Protein-Modified Nanocrystalline Diamond Thin Films for Biosensor Applications. *Nat. Mater.* **2004**, *3*, 736−742.
(9) Stavis, C.; Clare, T. L.; Butler, J. E.; Radadia, A. D.; Carr, R.; Zeng, H.; King, W. P.; Carlisle, J. A.; Aksimentiev, A.; Bashir, R.; Hamers, R. J. Surface Functionalization of Thin-Film Diamond for Highly Stable and Selective Biological Interfaces. *Proc. Natl. Acad. Sci. U.S.A.* **2011**, *108*, 983−988.
(10) Nebel, C. E.; Shin, D.; Rezek, B.; Tokuda, N.; Uetsuka, H.; Watanabe, H. Diamond and Biology. *J. R. Soc. Interface* **2007**, *4*, 439−461.
(11) Raymakers, J.; Haenen, K.; Maes, W. Diamond Surface Dunctionalization: From Gemstone to Photoelectrochemical Applications. *J. Mater. Chem. C* **2019**, *7*, 10134−10165.
(12) Hauf, M. V.; Grotz, B.; Naydenov, B.; Dankerl, M.; Pezzagna, S.; Meijer, J.; Jelezko, F.; Wrachtrup, J.; Stutzmann, M.; Reinhard, F.; Garrido, J. A. Chemical Control of the Charge State of Nitrogen-Vacancy Centers in Diamond. *Phys. Rev. B* **2011**, *83*, 081304.
(13) Bluvstein, D.; Zhang, Z.; Bleszynski Jayich, A. C. Identifying and Mitigating Charge Instabilities in Shallow Diamond Nitrogen-Vacancy Centers. *Phys. Rev. Lett.* **2019**, *122*, 076101.
(14) Rondin, L.; Dantelle, G.; Slablab, A.; Grosshans, F.; Treussart, F.; Bergonzo, P.; Perruchas, S.; Gacoin, T.; Chaigneau, M.; Chang, H.-C.; Jacques, V.; Roch, J.-F. Surface-Induced Charge State Conversion of Nitrogen-Vacancy Defects in Nanodiamonds. *Phys. Rev. B* **2010**, *82*, 115449.
(15) Ofori-Okai, B. K.; Pezzagna, S.; Chang, K.; Loretz, M.; Schirhagl, R.; Tao, Y.; Moores, B. A.; Groot-Berning, K.; Meijer, J.; Degen, C. L. Spin Properties of Very Shallow Nitrogen Vacancy Defects in Diamond. *Phys. Rev. B* **2012**, *86*, 081406.
(16) Loretz, M.; Pezzagna, S.; Meijer, J.; Degen, C. L. Nanoscale Nuclear Magnetic Resonance with a 1.9-nm-Deep Nitrogen-Vacancy Sensor. *Appl. Phys. Lett.* **2014**, *104*, 033102.
(17) Rosskopf, T.; Dussaux, A.; Ohashi, K.; Loretz, M.; Schirhagl, R.; Watanabe, H.; Shikata, S.; Itoh, K. M.; Degen, C. L. Investigation of Surface Magnetic Noise by Shallow Spins in Diamond. *Phys. Rev. Lett.* **2014**, *112*, 147602.
(18) Cui, S.; Hu, E. L. Increased Negatively Charged Nitrogen-Vacancy Centers in Fluorinated Diamond. *Appl. Phys. Lett.* **2013**, *103*, 051603.
(19) Stacey, A.; O'Donnell, K. M.; Chou, J.-P.; Schenk, A.; Tadich, A.; Dontschuk, N.; Cervenka, J.; Pakes, C.; Gali, A.; Hoffman, A.; Prawer, S. Nitrogen Terminated Diamond. *Adv. Mater. Interfaces* **2015**, *2*, 1500079.
(20) Chou, J.-P.; Retzker, A.; Gali, A. Nitrogen-Terminated Diamond (111) Surface for Room-Temperature Quantum Sensing and Simulation. *Nano Lett.* **2017**, *17*, 2294−2298.
(21) Kawai, S.; Yamano, H.; Sonoda, T.; Kato, K.; Buendia, J. J.; Kageura, T.; Fukuda, R.; Okada, T.; Tanii, T.; Higuchi, T.; Haruyama, M.; Yamada, K.; Onoda, S.; Ohshima, T.; Kada, W.; Hanaizumi, O.; Stacey, A.; Teraji, T.; Kono, S.; Isoya, J.; Kawarada, H. Nitrogen-Terminated Diamond Surface for Nanoscale NMR by Shallow Nitrogen-Vacancy Centers. *J. Phys. Chem. C* **2019**, *123*, 3594−3604.
(22) Körner, W.; Ghassemizadeh, R.; Urban, D. F.; Elsässer, C. Influence of (N,H)-Terminated Surfaces on Stability, Hyperfine Structure, and Zero-Field Splitting of NV Centers in Diamond. *Phys. Rev. B* **2022**, *105*, 085305.
(23) Fu, K.-M. C.; Santori, C.; Barclay, P. E.; Beausoleil, R. G. Conversion of Neutral Nitrogen-Vacancy Centers to Negatively Charged Nitrogen-Vacancy Centers through Selective Oxidation. *Appl. Phys. Lett.* **2010**, *96*, 121907.
(24) Kaviani, M.; Deák, P.; Aradi, B.; Frauenheim, T.; Chou, J.-P.; Gali, A. Proper Surface Termination for Luminescent Near-Surface NV Centers in Diamond. *Nano Lett.* **2014**, *14*, 4772−4777.
(25) Sangtawesin, S.; Dwyer, B. L.; Srinivasan, S.; Allred, J. J.; Rodgers, L. V. H.; De Greve, K.; Stacey, A.; Dontschuk, N.; O'Donnell, K. M.; Hu, D.; Evans, D. A.; Jaye, C.; Fischer, D. A.; Markham, M. L.; Twitchen, D. J.; Park, H.; Lukin, M. D.; de Leon, N. P. Origins of Diamond Surface Noise Probed by Correlating Single-Spin Measurements with Surface Spectroscopy. *Phys. Rev. X* **2019**, *9*, 031052.
(26) Fávaro de Oliveira, F.; Momenzadeh, S. A.; Wang, Y.; Konuma, M.; Markham, M.; Edmonds, A. M.; Denisenko, A.; Wrachtrup, J. Wrachtrup, Effect of Low-Damage Inductively Coupled Plasma on Shallow Nitrogen-Vacancy Centers in Diamond. *J. Appl. Phys. Lett.* **2015**, *107*, 073107.
(27) Schlipf, L.; Oeckinghaus, T.; Xu, K.; Dasari, D. B. R.; Zappe, A.; Fávaro de Oliveira, F.; Kern, B.; Azarkh, M.; Drescher, M.; Ternes, M.; Kern, K.; Wrachtrup, J.; Finkler, A. A Molecular Quantum Spin Network Controlled by a Single Qubit. *Sci. Adv.* **2017**, *3*, No. e1701116.
(28) Sushkov, A. O.; Chisholm, N.; Lovchinsky, I.; Kubo, M.; Lo, P. K.; Bennett, S. D.; Hunger, D.; Akimov, A.; Walsworth, R. L.; Park, H.; Lukin, M. D. All-Optical Sensing of a Single-Molecule Electron Spin. *Nano Lett.* **2014**, *14*, 6443−6448.
(29) Lovchinsky, I.; Sushkov, A. O.; Urbach, E.; de Leon, N. P.; Choi, S.; De Greve, K.; Evans, R.; Gertner, R.; Bersin, E.; Müller, C.; McGuinness, L.; Jelezko, F.; Walsworth, R. L.; Park, H.; Lukin, M. D. Nuclear Magnetic Resonance Detection and Spectroscopy of Single Proteins using Quantum Logic. *Science* **2016**, *351*, 836−841.
(30) Wolcott, A.; Schiros, T.; Trusheim, M. E.; Chen, E. H.; Nordlund, D.; Diaz, R. E.; Gaathon, O.; Englund, D.; Owen, J. S. Surface Structure of Aerobically Oxidized Diamond Nanocrystals. *J. Phys. Chem. C* **2014**, *118*, 26695−26702.
(31) Wang, X.; Ruslinda, A. R.; Ishiyama, Y.; Ishii, Y.; Kawarada, H. Higher Coverage of Carboxylic Acid Groups on Oxidized Single Crystal Diamond (001). *Diam. Relat. Mater.* **2011**, *20*, 1319−1324.
(32) Damle, V.; Wu, K.; De Luca, O.; Ortí-Casañ, N.; Norouzi, N.; Morita, A.; de Vries, J.; Kaper, H.; Zuhorn, I. S.; Eisel, U.; Vanpoucke, D. E. P.; Rudolf, P.; Schirhagl, R. Influence of diamond crystal orientation on the interaction with biological matter. *Carbon* **2020**, *162*, 1−12.
(33) Liu, K. S.; Henning, A.; Heindl, M. W.; Allert, R. D.; Bartl, J. D.; Sharp, I. D.; Rizzato, R.; Bucher, D. B. Surface NMR using Quantum Sensors in Diamond. *Proc. Natl. Acad. Sci. U. S. A.* **2022**, *119*, No. e2111607119.
(34) Xie, M.; Yu, X.; Rodgers, L. V. H.; Xu, D.; Chi-Durán, I.; Toros, A.; Quack, N.; de Leon, N. P.; Maurer, P. C. Biocompatible Surface Functionalization Architecture for a Diamond Quantum Sensor. *Proc. Natl. Acad. Sci. U. S. A.* **2022**, *119*, No. e2114186119.
(35) Kolkowitz, S.; Unterreithmeier, Q. P.; Bennett, S. D.; Lukin, M. D. Sensing Distant Nuclear Spins with a Single Electron Spin. *Phys. Rev. Lett.* **2012**, *109*, 137601.
(36) Müller, C.; Kong, X.; Cai, J.-M.; Melentijević, K.; Stacey, A.; Markham, M.; Twitchen, D.; Isoya, J.; Pezzagna, S.; Meijer, J.; Du, J. F.; Plenio, M. B.; Naydenov, B.; McGuinness, L. P.; Jelezko, F. Nuclear Magnetic Resonance Spectroscopy with Single Spin Sensitivity. *Nat. Commun.* **2014**, *5*, 4703.
(37) Sushkov, A. O.; Lovchinsky, I.; Chisholm, N.; Walsworth, R. L.; Park, H.; Lukin, M. D. Magnetic Resonance Detection of Individual Proton Spins Using Quantum Reporters. *Phys. Rev. Lett.* **2014**, *113*, 197601.
(38) Boss, J. M.; Chang, K.; Armijo, J.; Cujia, K.; Rosskopf, T.; Maze, J. R.; Degen, C. L. One- and Two-Dimensional Nuclear Magnetic Resonance Spectroscopy with a Diamond Quantum Sensor. *Phys. Rev. Lett.* **2016**, *116*, 197601.
(39) Cujia, K. S.; Boss, J. M.; Herb, K.; Zopes, J.; Degen, C. L. Tracking the Precession of Single Nuclear Spins by Weak Measurements. *Nature* **2019**, *571*, 230−233.

https://doi.org/10.1021/acs.nanolett.2c00533
Nano Lett. 2022, 22, 7294−7303

(40) Notsu, H.; Fukazawa, T.; Tatsuma, T.; Tryk, D. A.; Fujishima, A. Hydroxyl Groups on Boron-Doped Diamond Electrodes and Their Modification with a Silane Coupling Agent. *Electrochem. Solid-State Lett.* **2001**, *4*, H1.
(41) Ohta, R.; Saito, N.; Inoue, Y.; Sugimura, H.; Takai, O. Organosilane Self-Assembled Monolayers Directly Linked to the Diamond Surfaces. *J. Vac. Sci. Technol. A* **2004**, *22*, 2005−2009.
(42) Hernando, J.; Pourrostami, T.; Garrido, J. A.; Williams, O. A.; Gruen, D. M.; Kromka, A.; Steinmüller, D.; Stutzmann, M. Immobilization of Horseradish Peroxidase via an Amino Silane on Oxidized Ultrananocrystalline Diamond. *Diam. Relat. Mater.* **2007**, *16*, 138−143.
(43) Acres, R. G.; Ellis, A. V.; Alvino, J.; Lenahan, C. E.; Khodakov, D. A.; Metha, G. F.; Andersson, G. G. Molecular Structure of 3-Aminopropyltriethoxysilane Layers Formed on Silanol-Terminated Silicon Surfaces. *J. Phys. Chem. C* **2012**, *116*, 6289−6297.
(44) Naik, V. V.; Crobu, M.; Venkataraman, N. V.; Spencer, N. D. Multiple Transmission-Reflection IR Spectroscopy Shows that Surface Hydroxyls Play Only a Minor Role in Alkylsilane Monolayer Formation on Silica. *J. Phys. Chem. Lett.* **2013**, *4*, 2745−2751.
(45) Stine, R.; Cole, C. L.; Ainslie, K. M.; Mulvaney, S. P.; Whitman, L. J. Formation of Primary Amines on Silicon Nitride Surfaces: A Direct, Plasma-Based Pathway to Functionalization. *Langmuir* **2007**, *23*, 4400−4404.
(46) Asenath Smith, E.; Chen, W. How To Prevent the Loss of Surface Functionality Derived from Aminosilanes. *Langmuir* **2008**, *24*, 12405−12409.
(47) Vandenberg, E. T.; Bertilsson, L.; Liedberg, B.; Uvdal, K.; Erlandsson, R.; Elwing, H.; Lundström, I. Structure of 3-Aminopropyl Triethoxy Silane on Silicon Oxide. *J. Colloid Interface Sci.* **1991**, *147*, 103−118.
(48) Ziegler, J. F.; Ziegler, M. D.; Biersack, J. P. SRIM − The Stopping and Range of Ions in Matter (2010). *Nucl. Instrum. Methods Phys. Res. B: Beam Interact. Mater. At.* **2010**, *268*, 1818−1823.
(49) Hausmann, B. J.; Khan, M.; Zhang, Y.; Babinec, T. M.; Martinick, K.; McCutcheon, M.; Hemmer, P. R.; Lončar, M. Fabrication of Diamond Nanowires for Quantum Information Processing Applications. *Diam. Relat. Mater.* **2010**, *19*, 621−629.
(50) Zhu, D.; Bandy, J. A.; Li, S.; Hamers, R. J. Amino-Terminated Diamond Surfaces: Photoelectron Emission and Photocatalytic Properties. *Surf. Sci.* **2016**, *650*, 295−301.
(51) Coffinier, Y.; Szunerits, S.; Jama, C.; Desmet, R.; Melnyk, O.; Marcus, B.; Gengembre, L.; Payen, E.; Delabouglise, D.; Boukherroub, R. Peptide Immobilization on Amine-Terminated Boron-Doped Diamond Surfaces. *Langmuir* **2007**, *23*, 4494−4497.
(52) Wei, J. J.; Liu, J. L.; Chen, L. X.; Hei, L.-F.; Lv, F. X.; Li, Ch. M. Amination of Diamond Film by Ammonia Microwave Plasma Treatment. *Diam. Relat. Mater.* **2015**, *54*, 34−38.
(53) Torrengo, S.; Miotello, A.; Minati, L.; Bernagozzi, I.; Ferrari, M.; Dipalo, M.; Kohn, E.; Speranza, G. The Role of Oxygen in the One Step Amination Process of Nanocrystalline Diamond Surface. *Diam. Relat. Mater.* **2011**, *20*, 990−994.
(54) Wang, Q.; Kromka, A.; Houdkova, J.; Babchenko, O.; Rezek, B.; Li, M.; Boukherroub, R.; Szunerits, S. Nanomolar Hydrogen Peroxide Detection Using Horseradish Peroxidase Covalently Linked to Undoped Nanocrystalline Diamond Surfaces. *Langmuir* **2012**, *28*, 587−592.
(55) Chandran, M.; Shasha, M.; Michaelson, S.; Hoffman, A. Nitrogen Termination of Single Crystal (100) Diamond Surface by Radio Frequency N_2 Plasma Process: An *in-situ* X-Ray Photoemission Spectroscopy and Secondary Electron Emission Studies. *Appl. Phys. Lett.* **2015**, *107*, 111602.
(56) Yeh, J. J.; Lindau, I. Atomic Subshell Photoionization Cross Sections and Asymmetry Parameters: $1 \leq Z \leq 103$. *At. Data Nucl. Data Tables* **1985**, *32*, 1−155.
(57) Tanuma, S.; Powell, C. J.; Penn, D. R. Calculations of Electron Inelastic Mean Free Paths. *Surf. Interface Anal.* **2005**, *37*, 1−14.
(58) Graf, N.; Yegen, E.; Gross, T.; Lippitz, A.; Weigel, W.; Krakert, S.; Terfort, A.; Unger, W. E. S. XPS and NEXAFS Studies of Aliphatic and Aromatic Amine Species on Functionalized Surfaces. *Surf. Sci.* **2009**, *603*, 2849−2860.
(59) Baldwin, C. G.; Downes, J. E.; McMahon, C. J.; Bradac, C.; Mildren, R. P. Nanostructuring and Oxidation of Diamond by Two-Photon Ultraviolet Surface Excitation: An XPS and NEXAFS Study. *Phys. Rev. B* **2014**, *89*, 195422.
(60) Carr, H. Y.; Purcell, E. M. Effects of Diffusion on Free Precession in Nuclear Magnetic Resonance Experiments. *Phys. Rev.* **1954**, *94*, 630−638.
(61) Meiboom, S.; Gill, D. Modified Spin-Echo Method for Measuring Nuclear Relaxation Times. *Rev. Sci. Instrum.* **1958**, *29*, 688−691.
(62) Degen, C. L.; Reinhard, F.; Cappellaro, P. Quantum Sensing. *Rev. Mod. Phys.* **2017**, *89*, 035002.
(63) Pham, L. M.; DeVience, S. J.; Casola, F.; Lovchinsky, I.; Sushkov, A. O.; Bersin, E.; Lee, J.; Urbach, E.; Cappellaro, P.; Park, H.; Yacoby, A.; Lukin, M.; Walsworth, R. L. NMR Technique for Determining the Depth of Shallow Nitrogen-Vacancy Centers in Diamond. *Phys. Rev. B* **2016**, *93*, 045425.
(64) Herb, K.; Welter, P. Parallel Time Integration using Batched BLAS (Basic Linear Algebra Subprograms) Routines. *Comput. Phys. Commun.* **2022**, *270*, 108181.
(65) Degen, C. L.; Poggio, M.; Mamin, H. J.; Rettner, C. T.; Rugar, D. Nanoscale Magnetic Resonance Imaging. *Proc. Natl. Acad. Sci. U.S.A.* **2009**, *106*, 1313−1317.
(66) Mamin, H. J.; Oosterkamp, T. H.; Poggio, M.; Degen, C. L.; Rettner, C. T.; Rugar, D. Isotope-Selective Detection and Imaging of Organic Nanolayers. *Nano Lett.* **2009**, *9*, 3020−3024.
(67) Xue, F.; Weber, D. P.; Peddibhotla, P.; Poggio, M. Measurement of Statistical Nuclear Spin Polarization in a Nanoscale GaAs Sample. *Phys. Rev. B* **2011**, *84*, 205328.
(68) Grob, U.; Krass, M. D.; Héritier, M.; Pachlatko, R.; Rhensius, J.; Košata, J.; Moores, B. A.; Takahashi, H.; Eichler, A.; Degen, C. L. Magnetic Resonance Force Microscopy with a One-Dimensional Resolution of 0.9 Nanometers. *Nano Lett.* **2019**, *19*, 7935−7940.
(69) Myers, B. A.; Das, A.; Dartiailh, M. C.; Ohno, K.; Awschalom, D. D.; Bleszynski Jayich, A. C. Probing Surface Noise with Depth-Calibrated Spins in Diamond. *Phys. Rev. Lett.* **2014**, *113*, 027602.
(70) Fávaro de Oliveira, F.; Antonov, D.; Wang, Y.; Neumann, P.; Momenzadeh, S. A.; Häußermann, T.; Pasquarelli, A.; Denisenko, A.; Wrachtrup, J. Tailoring Spin Defects in Diamond by Lattice Charging. *Nat. Commun.* **2017**, *8*, 15409.
(71) Findler, C.; Lang, J.; Osterkamp, C.; Nesládek, M.; Jelezko, F. Indirect Overgrowth as a Synthesis Route for Superior Diamond Nano Sensors. *Sci. Rep.* **2020**, *10*, 22404.
(72) Krečmarová, M.; Gulka, M.; Vandenryt, T.; Hrubý, J.; Fekete, L.; Hubík, P.; Taylor, A.; Mortet, V.; Thoelen, R.; Bourgeois, E.; Nesládek, M. A Label-Free Diamond Microfluidic DNA Sensor Based on Active Nitrogen-Vacancy Center Charge State Control. *ACS Appl. Mater. Interfaces* **2021**, *13*, 18500−18510.
(73) Kayci, M.; Fan, J.; Bakirman, O.; Herrmann, A. Multiplexed Sensing of Biomolecules with Optically Detected Magnetic Resonance of Nitrogen-Vacancy Centers in Diamond. *Proc. Natl. Acad. Sci. U. S. A.* **2021**, *118*, No. e2112664118.
(74) Li, C.; Soleyman, R.; Kohandel, M.; Cappellaro, P. SARS-CoV-2 Quantum Sensor Based on Nitrogen-Vacancy Centers in Diamond. *Nano Lett.* **2022**, *22*, 43−49.
(75) Mzyk, A.; Ong, Y.; Ortiz Moreno, A. R.; Padamati, S. K.; Zhang, Y.; Reyes-San-Martin, C. A.; Schirhagl, R. Diamond Color Centers in Diamonds for Chemical and Biochemical Analysis and Visualization. *Anal. Chem.* **2022**, *94*, 225−249.

https://doi.org/10.1021/acs.nanolett.2c00533
Nano Lett. 2022, 22, 7294−7303